Band-to-band photorefraction

Germano Montemezzani, Philipp Dittrich, Peter Günter

Band-to-Band Photorefraction

Germano Montemezzani[1,2], Philipp Dittrich[1], and Peter Günter[1]

[1] Nonlinear Optics Laboratory, Swiss Federal Institute of Technology, Zürich (Switzerland)
[2] Present address: Laboratoire Matériaux Optiques, Photoniques et Systèmes, University of Metz and Supélec, Metz (France)
germano.montemezzani@metz.supelec.fr

1. Introduction

In conventional photorefraction, which is the matter of most of the chapters in this book series, the photoexcitation at the origin of the charge transport process occurs from mid-gap defect levels introduced by intentional or unintentional doping of the material being used. The doping level is usually moderate as compared to the intrinsic density of potentially available charges, which in the example of crystalline materials is of the order of the density of states at the top of the valence band or at the bottom of the conduction band. In the case of conventional photorefractive effects, the moderate doping level leads to a rather inefficient photoexcitation process and therefore to a rather slow photorefractive response. As discussed in detail in Chapter 3 of the second volume of this book series, the Maxwell dielectric time τ_{die} and the excitation time τ_{ex} are both inversely proportional to the photoexcitation rate and limit the response speed in different regimes. Therefore, for a given material, a significant enhancement of the response speed can only be achieved by improving in some way the efficiency of the photoexcitation process.

An effective way to increase the photoexcitation rate is to forget the dopants altogether and concentrate on phototransitions between the intrinsic levels across the band-gap of the material. These transitions are allowed if light of sufficient photon energy is used. Since every electron promoted to the upper mobile state will leave behind a hole in the lower mobile state, a photorefractive space-charge field will be created only if the motion of the electrons differs from the one of the holes, which is usually the case. This *interband photorefractive effect* presents characteristic features differing from those of the conventional effect, which involve specially the photoconductive properties and the dependence of the effect on light intensity. Besides the highly improved response speed, its other main advantage is the robustness of the involved gratings. The latter refers to the fact that a grating recorded by the interband photorefractive effect can be simultaneously read out by a very intensive light wave possessing a sub-band-gap photon energy without significantly erasing it. Speed and robustness open interesting perspectives of such interband photorefractive gratings for

parallel optical processing and optical wave manipulation tasks, such as dynamic splitters, switchers or filters.

This chapter will present the basics underlying interband photorefractive effects under cw illumination and highlight the main differences with respect to the conventional case. The considerations will be limited here to one-photon processes in bulk materials. It should be noted, however, that interband phototransitions may be induced also by two-photon processes at wavelengths significantly longer than the material band-edge. In semiconductors, such an approach can lead, for instance, to valuable information about two-photon, free-carrier, and deep-level cross sections [1]. Also, in semiconductors, a strong resonant electro-optic response can be obtained by illuminating the sample at wavelengths near the material band-edge and making use of the Franz-Keldysh effect [2, 3, 4] or, in structured materials, of the quantum-confined Stark effect [5, 6]. In contrast to the optical nonlinearity discussed in this chapter, these resonant effects are strong only in a limited wavelength range around the band-edge of the bulk semiconductor or of the multiple quantum-well structure. A vast literature exists on these subjects in semiconductor materials and the reader is referred to several excellent reviews [7, 8] and particularly to two chapters appearing in the second volume of this book series. The two-photon processes mentioned above have to be distinguished from two-photon excitation out of impurity levels which does not directly involve band-to-band transitions. With the help of short-pulse excitation, the latter approach was already used in the early stages of the photorefractive field to create stable holograms that could be read out nondestructively using a weaker intensity at the same wavelength, which is unable to create a significant amount of two-photon transitions [9, 10]. This is closely related to more recent investigations involving two-photons and two-colors hologram recording, performed with the aim to obtain quasi-fixed holograms for storage applications. The interested reader is referred to the next chapter in this volume.

The present chapter is structured in the following way. Section 7.2 will present the theoretical background with the help of a highly simplified model of the charge redistribution under interband photoexcitation conditions. The consequences for the photoconductivity, the space-charge fields, the grating dynamics, and the grating thickness will be discussed. Section 7.3 shortly discusses observed results in different materialsm, specifically $KNbO_3$, $LiTaO_3$ and $Sn_2P_2S_6$ while Section 7.4 describes some demonstrated potential applications for dynamic light-induced waveguides, switches and filters, and for parallel processing with the examples of incoherent-to-coherent conversion and optical correlation.

2 Interband Photorefraction with cw Recording Waves

This section describes very shortly the simplest theory and summarizes the main features of interband photorefractive effects recorded under cw illumination. The most important differences with respect to conventional photorefraction are pointed out.

2.1 Basic Equations

For interband photorefractive effects, the photoexciting light wavelength is in the high absorption spectral region for electronic resonances. Therefore the primary charge transfer mechanism is the phototransition of electrons between the valence and conduction band. In the simplest approximation, one may completely neglect all transitions involving mid-gap levels and write the material equations valid for an ideal trap-free material. This leads to a significant simplification in the mathematics. Here we will limit ourselves to the description of this limiting case. More complete models that consider the influence of recombination into mid-gap traps and photoexcitation out of them were given in [11]. It can be shown that for a sufficiently high cw illumination intensity, the solutions obtained with such models converge to the solutions of the *trap-free model* described here, which is based on following equations [11]

$$\frac{\partial n(\boldsymbol{r})}{\partial t} = gI(\boldsymbol{r}) - \gamma_{dir} n(\boldsymbol{r}) p(\boldsymbol{r}) + \frac{1}{e}\nabla \cdot \boldsymbol{J}_e(\boldsymbol{r}), \tag{7.1a}$$

$$\frac{\partial p(\boldsymbol{r})}{\partial t} = gI(\boldsymbol{r}) - \gamma_{dir} n(\boldsymbol{r}) p(\boldsymbol{r}) - \frac{1}{e}\nabla \cdot \boldsymbol{J}_p(\boldsymbol{r}), \tag{7.1b}$$

$$\boldsymbol{J}_e(\boldsymbol{r}) = en(\boldsymbol{r})\mu_{\mathrm{e}}\boldsymbol{E}(\boldsymbol{r}) + k_B T \mu_{\mathrm{e}} \cdot \nabla n(\boldsymbol{r}), \tag{7.1c}$$

$$\boldsymbol{J}_p(\boldsymbol{r}) = ep(\boldsymbol{r})\mu_{\mathrm{p}}\boldsymbol{E}(\boldsymbol{r}) - k_B T \mu_{\mathrm{p}} \cdot \nabla p(\boldsymbol{r}), \tag{7.1d}$$

$$\nabla \cdot \boldsymbol{E}(\boldsymbol{r}) = \frac{e}{\epsilon_{eff}\epsilon_0}(p(\boldsymbol{r}) - n(\boldsymbol{r})), \tag{7.1e}$$

where $\boldsymbol{r}$ is the position vector and all space-dependent variables are also time-dependent. Here $\boldsymbol{E}$ is the total internal electric field, ϵ_0 is the permittivity of vacuum, ϵ_{eff} is the (scalar) effective dielectric constant for the given photorefractive configuration (see Chapter 4 of this volume), e is the absolute value of the elementary charge, k_B is the Boltzmann-constant, and T is the absolute temperature. Further, n and p are the electron density in the conduction band and the hole density in the valence band, respectively, $\boldsymbol{J}_e$, $\boldsymbol{J}_p$, μ_{e} and μ_{p} are the electron and hole current densities and mobility tensors, respectively, γ_{dir} is the direct recombination constant between the two bands. Here the direct band-to-band photoexcitation process is expressed by the term $gI(\boldsymbol{r})$, where g is a photoexcitation constant given by $g = \alpha_{dir}/(\hbar k_0 c) = \alpha_{dir}/h\nu$, α_{dir} being the (intensity) absorption constant for the band-to-band transition, $k_0 = 2\pi/\lambda$ being the free space light wavevector, and $h\nu$ being the photon energy. By writing the photoexcitation term in this form, we have implicitly assumed that the photoexcitation process is isotropic with respect to the polarization of the interacting waves. If this is not the case, the light intensity I has to be replaced by a term containing a dissipated energy density, in a way similar as described in Chapter 4 for the case of conventional photorefraction.

The set of Eqs. (7.1a)–(7.1e) can be solved by taking the same kind of approach used for the equations describing the conventional photorefractive effect and discussed in other chapters of this book [12]. By assuming a sinusoidal light illumination, the space- and time-dependent variables are developed in a Fourier series that is being broken after the first harmonic term in space, a procedure that is well justified for small light modulation amplitudes.

2.2 Photoconductivity

Given a certain light intensity, the terms up to zero-order in the Fourier series give information about the average density of free electrons and free holes in the conduction and valence band, respectively.

Since Eqs. (7.1a)–(7.1e) neglect any charge recombination into trap levels and are symmetric with respect to electrons and holes, they predict an equally large free electron (n_0) and free hole (p_0) concentration; that is,

$$n_0 = p_0 = \sqrt{\frac{gI_0}{\gamma_{dir}}}. \tag{7.2}$$

The inclusion of recombination channels involving deep traps breaks this symmetry at low intensities (see [11]). However, it can be easily shown that for a sufficiently high light intensity, the limit above is always retrieved. Therefore, the free carrier concentration, and thus also the photoconductivity $\sigma_{ph} \equiv e(\mu_e n_0 + \mu_h p_0)$, are expected to increase with the square root of light intensity, as opposed to the linear increase expected for the simplest model of conventional photorefraction.

The deviation from the the relationship (7.2) at low intensities is shown in the example of Fig. 7.1, which shows measured photocurrent in pure $KNbO_3$ illuminated at the wavelength $\lambda = 364\,\text{nm}$. In this case, a nearly linear increase of the photocurrent is observed at intensities below $1\,\text{mW/cm}^2$, while above this limit, the behaviour expected from (7.2) is well reproduced.

2.3 Space-Charge Fields

Under a sinusoidal light intensity distribution of the type

$$I(\boldsymbol{r}) = I_0 \text{Re}[1 + m\exp(i\boldsymbol{K}\cdot\boldsymbol{r})], \tag{7.3}$$

the Eqs. (7.1a–7.1e) can be solved in a similar way as in the case of the single carrier band transport model. For the steady-state scalar space-charge field amplitude E_1 one obtains [11]

$$\boldsymbol{E}_1 = \hat{\boldsymbol{K}}\left\{-im\frac{[E_D(E_{Rh}-E_{Re}) - iE_0(E_{Re}+E_{Rh})]E_{qf}}{[(2E_{qf}+E_D)(E_D+E_{Re}+E_{Rh})+E_0^2] + iE_0[E_{Re}-E_{Rh}]}\right\}, \tag{7.4}$$

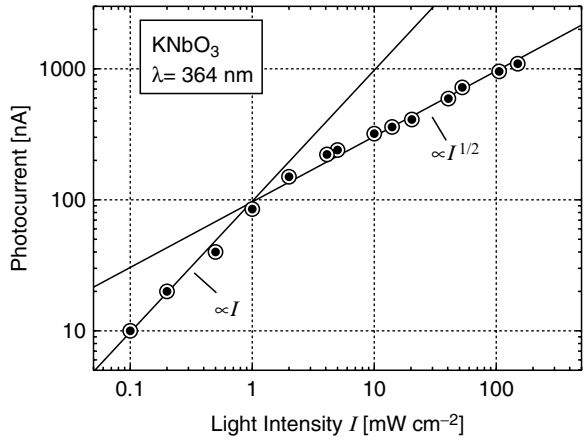

FIGURE 7.1. Photocurrent as a function of light intensity under interband illumination of $KNbO_3$. In the low intensity regime, the photocurrent increases linearly and charge recombination in deep traps plays a major role. In the high intensity regime, the photocurrent increases with the square root of light intensity and interband transitions dominate the process. (After [13])

where $\hat{\boldsymbol{K}}$ is the unit vector in direction of the grating vector $\boldsymbol{K}, E_0$ is the projection of an externally applied electric field in direction $\hat{\boldsymbol{K}}$, and $E_D \equiv |\boldsymbol{K}| k_B T/e$ is the diffusion field. The fields E_{qf}, E_{Re} and E_{Rh} are less familiar,

$$E_{qf} \equiv \frac{e}{\epsilon_0 \epsilon_{eff} |\boldsymbol{K}|} n_0 \tag{7.5}$$

is the free charge limiting field and stays in full analogy with space-charge limiting field E_q found in conventional photorefraction, while

$$E_{Re} \equiv \frac{1}{|\boldsymbol{K}| \mu_e} \gamma_{dir} p_0 \tag{7.6}$$

and

$$E_{Rh} \equiv \frac{1}{|\boldsymbol{K}| \mu_p} \gamma_{dir} n_0 \tag{7.7}$$

are the electron and hole recombination fields, respectively. Their magnitude can be interpreted as the average internal electric fields in which electrons (or holes) drift for an average distance $(K)^{-1} = \Lambda/2\pi$ before a recombination to the other band takes place. The scalar mobilities μ_e and μ_p in (7.6) and (7.7) correspond to the projection of the electron and hole mobility tensors along the direction $\hat{\boldsymbol{K}}$, as described in Chapter 4 of this volume.

Fig. 7.2 shows the typical dependence of the space-charge field amplitude on grating spacing for the interband case. At long grating spacings, one finds a saturation value in presence of an applied field of $E_1 = mE_0/2$, which is half as big with respect to the case of conventional photorefractive effects. The reason for this is the quadratic recombination process leading to relationship (7.2) for the free charge density; as a consequence, the modulation amplitude of the photoexcited charges is only half as big as the one of the light intensity. Another big difference with the conventional photorefraction is the behavior at small grating spacings Λ. While in the conventional case the space-charge field rises proportional to Λ, in interband photorefraction the initial rise is proportional to Λ^3. This is due to the fact that not only the free-carrier limiting field E_{qf} is giving a limitation to the space-charge field amplitude, but also the recombination fields E_{Re} and E_{Rh}. The overlinear increase of $\mathrm{Im}(E_1)$ with grating spacing was confirmed experimentally in pure $KNbO_3$ by means of interband two-

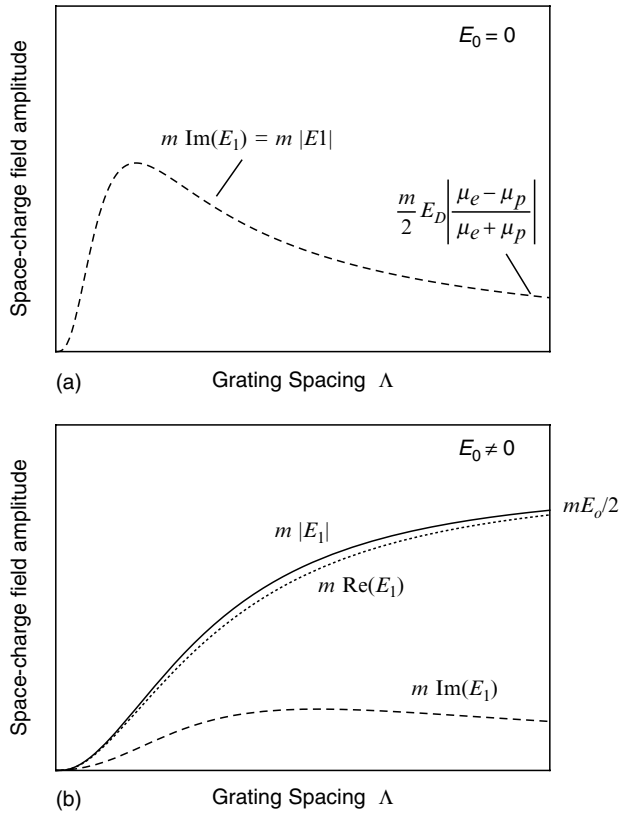

FIGURE 7.2. Dependence of space-charge field amplitude on grating spacing for interband photorefractive effects in absence of deep traps (4). a) No applied field; b) With externally applied field.

wave mixing investigations [11, 14]. Figure 7.2 (a) also shows that in absence of an external field the space-charge field is bound by the function $(m/2)E_D|(\mu_e - \mu_p)/(\mu_e + \mu_p)|$, therefore, as expected, no space-charge field can build up in this regime if the electron and hole mobilities are the same.

The role of the pseudo-fields E_{qf}, E_{Re} and E_{Rh} merits some additional discussion. A significant space-charge field amplitude can be reached only if E_{qf} and at least one among the recombination fields E_{Re} and E_{Rh} are large enough, say, of the order of 1 kV/cm. Looking at Eq. (7.5) one recognizes that the requirement of a large field E_{qf} means nothing else than the charge density n_0 should be large enough to sustain the modulated space-charge field. The second condition implies that at least one of the carrier mobilities should be small enough so that, before recombination, the carrier is prevented from drifting too far as compared to the fringe distance. If the drift or diffusion distances are too long, the carrier looses coherence with the illuminating light distribution and the resulting space-charge field modulation amplitude decreases. In pure $KNbO_3$, the limitations due to E_{qf}, E_{Re} and E_{Rh} normally become important only at grating spacings below $\sim 0.5\,\mu$m. In general, significant space-charge field amplitudes at submicron grating spacing can be easily achieved already for an illuminating intensity of the order of few tens of mW/cm^2($\lambda = 364$ nm). For experiments where the typical distances are larger ($5 - 10\,\mu$m), such as the dynamic waveguides described in Section 7.4.3, the constraints on E_{qf}, E_{Re} and E_{Rh}, and thus on the illumination intensity, are even less stringent.

2.4. Grating Dynamics

The dynamic behavior of interband photorefractive effects is more complex than the one for the conventional case. In the latter situation, the carriers are photoexcited from mid-gap levels and the equilibrium average carrier density in the conduction (or valence) band is reached in a time, which is short as compared to the build-up time of the space-charge field. This is no longer true for interband gratings. The large free carrier density has to build up first and the time required for this process may be comparable or even longer than the characteristic time constants for the charge redistribution process, such as the dielectric time $\tau_{die} \equiv e\mu n_0/(\varepsilon_0\varepsilon_{eff})$ or the diffusion time $\tau_D \equiv e/(K^2 k_B T \mu)$ for electrons or holes. As discussed in more depth in [11], it is clear that the space-charge field cannot reach a steady-state before the average charge density $n_0(t)$ also does so. Upon switching on the illumination at time $t = 0$, in absence of deep traps, the latter grows approximately as

$$n_0(t) = n_0(t = \infty)\ \tanh\,(\Gamma_{dir} t), \tag{7.8}$$

where $n_0(t = \infty)$ is the steady-state value given by (7.2) and

$$\Gamma_{dir} \equiv \gamma_{dir} n_0(t = \infty) = \sqrt{g I_0 \gamma_{dir}} \tag{7.9}$$

is the recombination rate that governs the charge density build-up. Correspondingly, upon switching off the illumination, the free charge density initially decays in the dark as

$$n_0(t) \equiv n_0(t=0)\frac{1}{1+\Gamma_{dir}t}. \tag{7.10}$$

In pure $KNbO_3$ at wavelengths around 350 nm, the time rate Γ_{dir} is typically of the order of $(10\,\mu s)^{-1}$ for illumination intensities of the order of $100\,mW/cm^2$. As will be shown later, the photorefractive response time in the interband regime is also in the $10-100\,\mu s$ range, which is faster by at least two orders of magnitude with respect to the typical speed of the same material in the conventional photorefractive regime.

Eqs. (7.8) and (7.10) describe the build-up and decay of the average charge density and therefore do not consider any charge transport issues that are important to describe the formation of the space-charge field. An exact analytical solution of the dynamic Eqs. (7.1a)–(7.1e) is made difficult by the above time dependence of n_0. Therefore we rely here on a simpler approach that assumes that the build up of the modulated space-charge field starts from a state in which the average free carrier density is already established. In other words, at time $t=0$, only the modulation m in (7.3) is being switched on. Following [15], the dynamic solution of the set (7.1a)–(7.1e) takes the form

$$\boldsymbol{E}_1(t) = \boldsymbol{E}_{1,sat}\{1-\frac{1}{2}[(1-B/C)e^{-\Gamma_1 t}+(1+B/C)e^{-\Gamma_2 t}]\}, \tag{7.11}$$

where $\boldsymbol{E}_{1,sat}$ corresponds to the steady-state solution (7.4) and

$$B \equiv (E_D+E_{qf})(E_{Re}+E_{Rh})+iE_0(E_{Re}-E_{Rh})+2E_{Re}E_{Rh}, \tag{7.12}$$

$$C \equiv \{[(E_D+E_{qf})(E_{Re}-E_{Rh})-iE_0(E_{Re}+E_{Rh})]^2+4E_{Re}E_{Rh}(E_{qf}-E_{Re})(E_{qf}-E_{Rh})\}^{1/2}. \tag{7.13}$$

The exponential time rates $\Gamma_{1,2}$ are given by

$$\Gamma_{1,2} = \frac{\Gamma_{dir}}{2E_{Re}E_{Rh}}(B \mp C). \tag{7.14}$$

Fig. 7.3 shows the dependence of the time rates Γ_{dir}, Γ_1 and Γ_2 on light intensity. Note that in general, depending on material parameters, the time rates Γ_1 and Γ_2 may be either larger (as in the case represented here) or smaller than the direct recombination rate Γ_{dir}. Note also that despite of this, in the former case, if the experiment starts from an unilluminated crystal, the grating build-up time is still limited by the time needed to build up the average charge distribution and therefore, cannot be faster than $1/\Gamma_{dir}$.

Fig. 7.3 contains also experimental data from [16] which confirm the expected square-root dependence of time rate on intensity. It has to be noticed

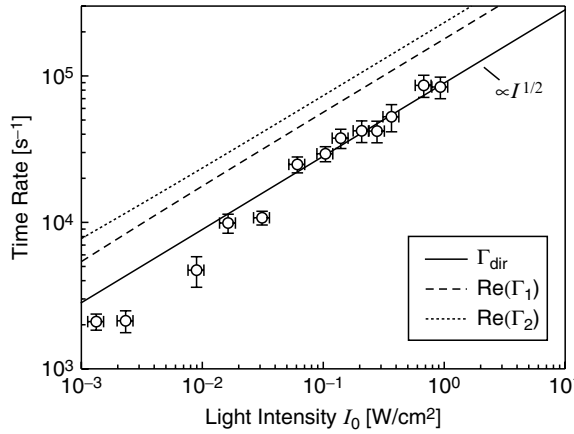

FIGURE 7.3. Intensity dependence of the direct recombination rate Γ_{dir} and of the photorefractive time rates Γ_1 and Γ_2 according to Eqs. (7.9) and (7.14). The parameters used for the plots are $g = 10^{24}\ \mathrm{J^{-1}m^{-1}}$, $\gamma_{dir} = 8 \cdot 10^{-19}\,\mathrm{m^3/s}$, $\mu_e = 10^{-9}\,\mathrm{m^2/(Vs)}$, $\mu_h = 3 \cdot 10^{-9}\,\mathrm{m^2/(Vs)}$, $\Lambda = 4.7\,\mu\mathrm{m}$ and $E_0 = 2.2\,\mathrm{kV/cm}$. The points show corresponding measured time rates in pure $KNbO_3$ under illumination at the wavelength $\lambda = 351\,\mathrm{nm}$ [16], which are found to follow well the expected square root dependence on intensity.

that the value of the recombination constant γ_{dir} has been adjusted in such a way as to normalize the value of Γ_{dir} to the experimentally measured data.

It is worth noting that in some limits, the time rates Γ_1 and Γ_2 may be expressed in a simpler form. First, for small grating spacings ($\Lambda \to 0$), the rates Γ_1 and Γ_2 converge toward the diffusion rates for holes and electrons $\Gamma_{Dh} \equiv k_B T K^2 \mu_p / e$ and $\Gamma_{De} \equiv k_B T K^2 \mu_e / e$, respectively. In the opposite limit, for large grating spacings Λ, one has ($E_D \ll E_{qf}$) and for the case where the free charge limiting field is the dominating quantity ($E_{qf} \gg E_{Re}, E_{Rh}$) the expression (7.11) takes the simpler form

$$\boldsymbol{E}_1(t) = -im\hat{\boldsymbol{K}}\frac{E_D}{2}\frac{\mu_p - \mu_e}{\mu_p + \mu_e}\{1 - \exp[-(\Gamma_{die} + \Gamma_{dih})t]\}, \tag{7.15}$$

where $\Gamma_{die} \equiv (e\mu_e n_0/\epsilon_0\epsilon_{eff}) = (\tau_{die})^{-1}$ is the dielectric rate for electrons and Γ_{dih} is the corresponding dielectric rate for holes. Eq. (7.15) is valid for $E_0 = 0$. Therefore, multiple measurements of the time dynamics in the latter regime allow the determination of the ratio of the effective bipolar mobility μ_p/μ_e along the different crystallographic directions, as performed in [13].

2.5. Grating Thickness

For conventional photorefractive effects, the thickness of the recorded grating usually correspond to the thickness of the nonlinear sample being used. Since the incident recording light is being strongly absorbed, this is no longer true for

interband photorefraction. For the ideal "trap-free" case (7.2) and (7.4) predict that the space-charge field should depend on the square root of the light intensity and thus should decay exponentially inside the sample. This behaviour can be effectively observed near the surface where the light intensity is large and interband processes dominate over processes involving the residual deep traps. For specific situations, such as in the case where the sample is flooded by an intense sub-bandgap light [11], the exponential decay can extend over longer distances. However, in the general case, the grating strength departs from the exponential decay at depths where the recording intensity is so low that the carrier recombination into deep traps is dominating. The total extension of the grating reaches the depth where the remaining nonabsorbed photons are still able to create a photoconductivity larger or equal to the material dark conductivity. This depth can largely exceed the $1/\alpha$ level of the typical decay depth of the light intensity. For instance, in $KNbO_3$ at typical intensities of $100\,mW/cm^2$($\lambda = 364\,nm$, *c*-polarized light), the grating is found to extend until about $200\,\mu m$ below the surface. Since the corresponding intensity absorption constant is $\alpha_c \approx 550\,cm^{-1}$, this depth corresponds to about 10 times the $1/\alpha$ level.

As will be seen also later, experimental evidence show that in general, the crystal contains two distinct regions, one close to the surface where the grating is dominated by free charges, and a deeper one where trapped charges dominate. The position of the transition region between the two regions depends on intrinsic and extrinsic properties of the sample (purity, doping level, ...), on wavelength and polarization, and, of course, on light intensity. Detailed investigations on the influence of light intensity on grating shape was performed in [15].

3. Materials

It has to be expected that any electro-optic photoconducting crystal should exhibit interband photorefractive effects when illuminated with light whose photons have an energy exceeding the band-gap. For oxide type crystals typically used in conventional photorefraction, such as lithium niobate ($LiNbO_3$), potassium niobate ($KNbO_3$), and lithium tantalate ($LiTaO_3$), for example, the high absorption spectral region lies in the ultraviolet. But materials exhibiting interband photorefraction also in the visible spectral range are also available, e.g., tin hypothiodiphosphate ($Sn_2P_2S_6$, SPS).

In this section, we will shortly summarize the main characteristics of band-to-band photorefractive gratings recorded in the crystals $KNbO_3$, $LiTaO_3$, and $Sn_2P_2S_6$. Before starting, let us shortly recall that holographic investigations of the interband photorefractive effect are typically performed in two kinds of geometries: The longitudinal geometry, where the planes of incidence of the recording waves and of the read-out wave is the same, and the transverse geometry, where the two planes of incidence are perpendicular to each other. In the latter case, the read-out wave propagates parallel to the input surface of the recording beams and can be used to probe the grating at a well defined depth.

3.1. *Potassium Niobate (*$KNbO_3$*)*

Potassium niobate has a room temperature band-gap energy of 3.3 eV, therefore near ultraviolet light in the region of 350 nm to 365 nm leads to direct transitions between the valence band (related to the 2*p* orbitals of the oxygen ions) and the conduction band (related to the 4*d* orbitals of the Nb ions). The interband photorefractive properties of nominally pure $KNbO_3$ under illumination in the above mentioned spectral range were studied in Refs. [11, 13, 15–19]. Here we mention solely the most relevant features observed under cw illumination at the wavelengths 364 and 351 nm.

- The photoconductivity deviates from a linear dependence on light intensity for intensities of the order of $1\,\mathrm{mW/cm^2}$. Above this level, one reaches a regime with square root dependence (compare Fig. 7.1), an indication of interband effects.
- The interband gratings are composed of two principal components. The modulated charges giving rise to the first one are energetically located in the two bands and in shallow trap levels with fast thermal exchange with the bands. This component dominates for local light intensities above $50\,\mathrm{mW/cm^2}$ ($\lambda = 364\,\mathrm{nm}$) and is referred to as the *band grating*. The second component is composed of a carrier modulation in deep trap levels and is hence referred to as the *trap grating*. It dominates for local light intensities below $0.1\,\mathrm{mW/cm^2}$ and therefore it is the dominant component far enough from the entrance surface illuminated by the UV light. The average amplitude of the first grating component is about 5 to 10 times stronger than the one of the second one. In undoped crystals and in absence of externally applied electric fields, the two components are mutually phase shifted by π, which is supported by several pieces of evidence.

    (a) Direct depth resolved Bragg diffraction investigations in transverse geometry [11] show a minimum of diffraction efficiency at an intermediate depth for which band and trap grating have a comparable amplitude but cancel each other;
    (b) Off-Bragg angle Bragg diffraction investigations in longitudinal geometry [15] evidence the interesting and expected feature that at steady-state the maximum of diffraction efficiency is not observed at the Bragg angle, but at a nearby angle for which the destructive interference between the waves diffracted off the band and the trap grating turns to a constructive interference. This is illustrated in Fig. 7.4, which shows the angular dependence of the diffraction efficiency η (rocking curve) for various recording intensities in a $47\,\mu\mathrm{m}$ thick sample. Thus the grating evolution leads to very interesting time dynamics of the rocking curve measured in longitudinal geometry, as discussed in detail in [15]. As a result, the curve $\eta(t)$ shows a complex behavior that strongly depends on the

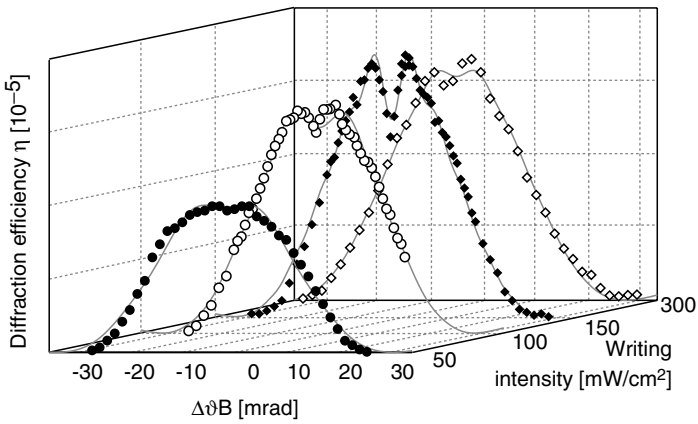

FIGURE 7.4. Measured internal angular selectivity of the diffraction efficiency for isotropic Bragg diffraction obtained in a 47 μm thin sample of $KNbO_3$ for different ultraviolet writing intensities ($\lambda = 364$ nm, grating spacing $\Lambda = 0.5\,\mu$m, grating vector along the c axis). The modulation depth is $m = 0.2$ and all the light beams are p-polarised. The solid lines are calculated from a simple model involving two grating components. See [15] for details.

light intensity (see Fig. 7.5) and on the angular deviation with respect to the Bragg angle. Despite the apparent complexity of the behavior, the dynamics can be satisfactorily modeled by considering solely the evolution of the two grating components discussed above, being displaced in space and in phase [15]. Note also in this respect, that if the intensity is large enough so that the band grating component dominates the diffraction, the slow evolution of the trap grating component loses importance and the dynamics measured in longitudinal geometry becomes simpler.

(c) The effective UV two-wave mixing gain coefficient has opposite signs for low and high wave intensities [15] as seen in Fig. 7.6. The fitted curves show that the trap-free model of Section 7.2.1 describes well the behaviour of the photorefractive gain at large light intensities, where the band grating dominates. However, this model cannot predict the observed zero crossing at low intensities. Inclusion of the charges trapped in deep levels is necessary. A highly simplified model of this kind was shown to correctly predict the observed transition with increasing light intensity [18].

- The average refractive index change modulation Δn obtained by the interband photorefractive effect is few times 10^{-5} and is of the same order of magnitude to what can be reached by conventional photorefractive effects in the same material.
- While the grating component stored in deep traps is affected by below bandgap visible illumination, the free carrier grating component is not. There-

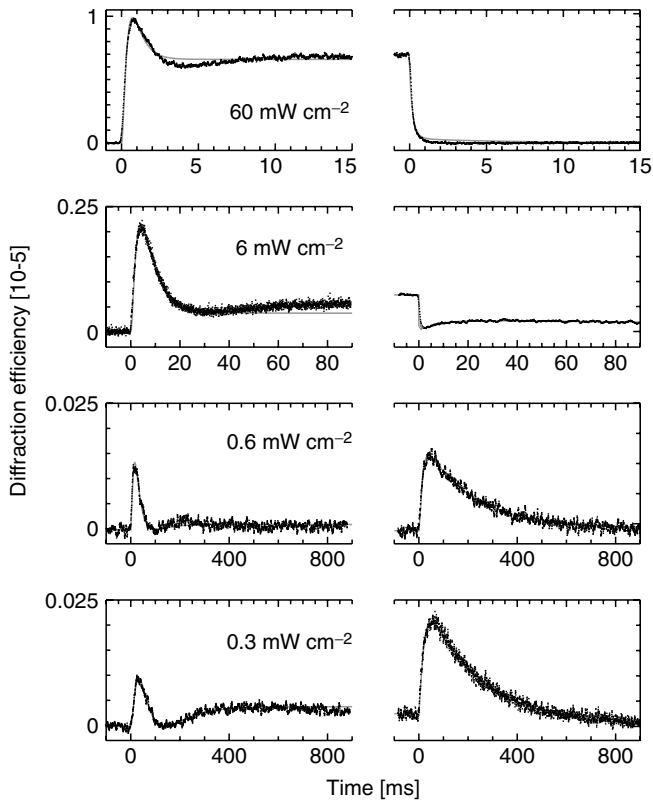

FIGURE 7.5. Intensity dependence of the dynamics of the diffraction efficiency measured in longitudinal geometry during the build-up (left) and the dark decay (right) obtained in a 47 μm thin sample of $KNbO_3$ for a fixed angle of incidence very close to the exact Bragg angle ($\Delta\vartheta < 2$ mrad). The oscillating dynamics is due to the interference between a fast band grating close to the front surface and a slower trap grating deeper inside the sample. The gray lines are calculated according to a simple model involving the evolution of these two gratings, as discussed in detail in [15].

fore, the near surface grating is extremely robust against optical erasure at wavelengths longer than those used for recording. In $KNbO_3$, it has been shown that incoherent visible light more than five orders of magnitude more intense than the ultraviolet recording beams does not significantly affect the free carrier component of the grating.

- At the intensity of 1 W/cm^2, the fast grating component shows a build-up and decay time of about 10 μs for $\lambda = 351$ nm and *b*-polarized light, where the intensity absorption constant is $\approx 5500\,\mathrm{cm}^{-1}$. This response time is increased by less than a factor of 4 for $\lambda = 364$ nm and *c*-polarized light, which are associated with a 10 times lower intensity absorption constant of $540 \pm 50\,\mathrm{cm}^{-1}$. As predicted by theory, the response time depends inversely

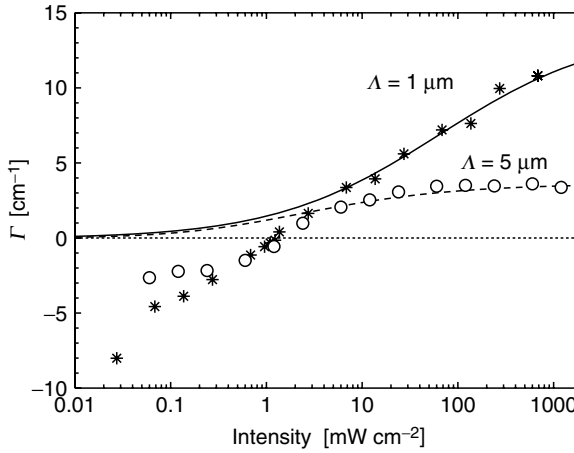

FIGURE 7.6. Intensity dependence of two-wave mixing gain for interband photorefraction in $KNbO_3$. The curves show the behavior predicted by "trap-free" model of the interband photorefractive effect (Eq. (7.4)). The zero-crossing point at the intensity of about 1 mW/cm^2 is not predicted by Eq. (7.4) and is due to the fact that at low intensity, a deep trap grating being out of phase by 180 degrees with respect to the free charge grating becomes the dominant component. Electrons are the dominant charge carriers at low intensities (electron-type conductivity dominates) while at large intensities, the conductivity is dominated by hole motion. $\lambda = 364$ nm, grating vector $||c$-axis, wave polarization in the bc-plane, modulation index $m = 0.11$. After [15].

proportional to the square root of light intensity (see Fig. 7.3). Note that the response times for conventional photorefraction in $KNbO_3$ range typically between ≈ 1 ms and few seconds depending on doping and chemical treatment. These are about two to six order of magnitude slower than the interband photorefractive gratings.

- For most samples, at typical intensities of 100 mW/cm^2($\lambda = 364$ nm, c-polarization), the grating is found to extend until about 200 μm below the illuminated surface, that is about 10 times the $1/2\alpha$ level. The maximum depth can be characterized by the point where the remaining nonabsorbed photons are still able to create a photoconductivity larger than the material dark conductivity. Therefore, as expected, the grating depth depends on light intensity, polarization, and wavelength. The position of the border between the two regions mutually dominated by the free carrier grating components and by the trapped grating component also depends on these quantities as well as on intrinsic and extrinsic properties of the sample (purity, doping level, ...) [15]. For conditions under which the trapped grating is not being significantly erased, the point at which the two gratings components have the same amplitude (but opposite sign) can extend up to about 100 μm below the surface.
- In the framework of the simple model presented in Section 7.2, all measurements in pure samples are consistent with an effective mobility for the

slowest carrier (electrons) slightly smaller than $10^{-5}\,cm^2/(Vs)$. This small value is given by a trap limiting effect due to carriers falling into shallow trap levels (mainly oxygen vacancies) in thermal equilibrium with the band. The effect of shallow traps is not explicitly included in the model of Section 7.2 and the band grating is in reality a grating induced by carriers sitting in the pseudo-band formed by the true band and the nearby shallow levels [11, 14].

- In principle, due to the strong absorption of the UV light, thermal effects such as direct thermooptic gratings [20], thermoelectric gratings [21], or gratings induced by pyroelectric space-charge fields [22, 23] could also give a contribution to the observations in diffraction experiments. However, direct experimental verification in several different geometries as well as theoretical estimations of the size of the effects based on the known material parameters show that none of these effects give a significant contribution at the cw intensities up to $\approx 1\,W/cm^2$ relevant for our investigations. Attempts performed with the aim to detect a possible presence of surface gratings using a reflection type geometry showed that also this effect is negligible.

3.2 Lithium Tantalate ($LiTaO_3$)

Due to its wide band-gap, lithium tantalate ($LiTaO_3$) is a promising material for short-wavelength holographic data storage and dynamic holography. The renewed interest in this materials is driven mostly by the successful growth of near-stoichiometric crystals, i.e. crystals with a composition very close to stoichiometry [24, 25, 26]. Compared to congruently grown $LiTaO_3$, near-stoichiometric $LiTaO_3$ shows a significant reduction of optical damage in the visible and an enhancement of the photosensitivity and of the diffusion-type photorefractive effect in the near ultraviolet [27, 28, 29]. Further, the absorption edge is shifted from about 275 nm for congruent $LiTaO_3$ toward about 260 nm [30]. It has been shown that for near stoichiometric $LiTaO_3$, the two-wave mixing gain coefficient is doubled compared to congruent $LiTaO_3$ at the UV wavelength $\lambda = 364\,nm$. At the same time, the typical photorefractive build-up and decay time constants are decreased by a factor of five [28]. Further, a distinct reduction of the saturated space-charge field is observed, which is due to a larger increase in the photoconductivity relative to the photogalvanic effect [27, 29].

Reviews about the conventional photorefractive properties of congruent and stoichiometric $LiTaO_3$ can be found in two chapters in the second volume of this book series. In the following, we will summarize the main properties of near stoichiometric pure and Mg doped $LiTaO_3$ regarding interband photorefraction [31, 32]. Investigations were performed at the deep UV wavelength $\lambda = 257\,nm$, a wavelength lying lower than the absorption edge of $LiTaO_3$.

- As for $KNbO_3$, the photoconductivity of near stoichiometric $LiTaO_3$ deviates from a linear dependence on light intensity for intensities of the order of $10\,mW/cm^2$.

- In analogy to $KNbO_3$, the presence of a band grating and of a trap grating could be identified and are also found here to be mutually out-of-phase. The first component reaches approximately from the surface until the depth d_b at which therecording UV intensity equals approximately the characteristic intensity I_c separating the linear and square root intensity regimes of the photoconductivity. Because of the exponential decrease of the UV light inside the crystal, this transition depth is given by $d_b \cong \alpha_{UV}^{-1} \ln(I_0/I_c)$. The second component extends approximately from the depth d_b until the depth at which the light intensity equals the dark intensity I_d. The latter is defined as the intensity where the induced photoconductivity equals the dark conductivity. The thickness of this second component is given approximately by $d_t \cong \alpha_{UV}^{-1} \ln(I_c/I_d)$. A direct, depth resolved observation of these two grating components by diffraction measurements in transverse geometry is shown in Fig. 7.7.
- The partial compensation between band and trap grating components can be undone by optically erasing the trap grating component using an intense nonresonant illumination unable to induce interband phototransitions. A significant increase of diffraction efficiency in longitudinal geometry is observed under such illumination conditions.
- Typical time constants for the interband effects for pure near-stoichiometric $LiTaO_3$ are in the order of a few tens of milliseconds for UV light intensities of about $100\,mW/cm^2$, three orders of magnitude faster than the time constants reported previously for lithium tantalate [28].
- It is well known that Mg ions act as compensators for intrinsic defects related to the deviation from stoichiometry in crystals of $LiNbO_3$ and $LiTaO_3$ [33, 34, 35, 36]. This compensation results in an increased photoconductivity and

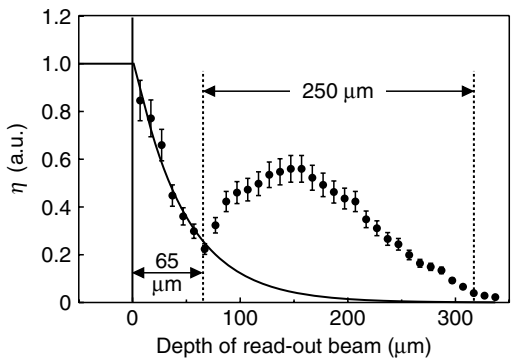

FIGURE 7.7. Bragg diffraction efficiency η as a function of the depth of the read-out beam d beneath the illuminated crystal surface, which is indicated by the solid vertical line at $d = 0\,\mu m$. The region $0 \leq d \leq 65\,\mu m$ is characterized by a dominant band grating. Its strength follows the exponential decrease ($\alpha = 450\,cm^{-1}$) of the UV intensity inside the crystal, indicated by the solid curve. The trap grating is dominant at larger depths, as recognized by the structure with its maximum at approximately $150\,\mu m$. The UV intensity at the crystal surface was $I_{UV} = 140\,mW/cm^2$.

a significantly reduced optical damage in Mg-doped samples as compared to congruently grown undoped samples. In the same way, in near-stoichiometric crystals, inclusions of a small amount of Mg helps compensating the remaining smaller amount of intrinsic defects. Recently it has been demonstrated that Mg doping (1 mol %) of near-stoichiometric $LiTaO_3$ increases the response rate of interband photorefractive gratings by a factor of 20 compared with the one in undoped crystals [32]. For UV light intensities larger than $500\,mW/cm^2$, the response time is faster than one millisecond. Note that in the near UV ($\lambda = 351\,nm$), a sensitivity enhancement by doping with Mg has been also demonstrated recently for lithium niobate crystals [37] in the conventional photorefractive regime.

The high spatial resolution of UV holography and the present response speed of less than one millisecond in Mg-doped near stoichiometric $LiTaO_3$ are such that applications of this type of crystals for the realization of high resolution real-time optical processing elements appear promising. Integrated optical functions that can be dynamically modified can also potentially be realized in this technologically very important crystal by means of interband photorefraction.

3.3. *Tin Hypothiodiphosphate,* $Sn_2P_2S_6$

Tin hypothiodiphosphate ($Sn_2P_2S_6$, SPS) is a ferroelectric crystal with large electro-optic coefficients [38] and a moderate band-gap energy of 2.3 eV. In the conventional sense, this material exhibits very good photorefractive properties in the red and near infrared spectral range [39, 40, 41, 42, 43, 44]. More detailed information about this material and its properties in connection with conventional photorefractive effects can be found in Chapter 9 of the second volume of this book series.

Since blue and green light are being strongly absorbed, SPS is suitable for hologram recording via interband photorefraction using visible light. Here we summarize some of the observations in this regime [45, 46, 47].

- For the wavelengths 514 and 488 nm, which are well within the interband absorption regime, the photoconductivity σ_{ph} follows well the square-root dependence on light intensity predicted from (7.2) for incident intensities larger than few mW/cm^2. The same is true for the wavelength $\lambda = 532\,nm$, which is at the edge of the absorption band, but only at elevated temperatures of about 50°C [47]. At this temperature and wavelength, the absorption constant exceeds $100\,cm^{-1}$ (X-polarization) and is increased by more than a factor of 4 with respect to room temperature, where the photoconductivity behavior evidences a mixed regime. For incident intensities I well below $1\,mW/cm^2$, two kinds of behaviors have been observed depending on crystal sample. Either a linear regime where σ_{ph} depends linearly on I (as for $KNbO_3$ and $LiTaO_3$), or a regime where the photoconductivity tends to approach a nearly constant plateau with a very weak dependence on intensity [48]. The latter behavior is expected if one of the conducting bands is being charged

with carriers as a result of a highly asymmetrical level of carrier exchange between the two bands and deep impurities [11].

- The refractive index change induced associated with interband photorefractive gratings in $Sn_2P_2S_6$ can reach few times 10^{-4} at $\lambda = 514\,\text{nm}$ and intensities exceeding $500\,\text{mW/cm}^2$, as confirmed by Bragg diffraction angular dependent measurements in longitudinal geometry and recent beam coupling investigations in thin samples [48].
- The contribution of possible mechanisms other than the photorefractive effect, such as absorption gratings, space-charge gratings induced by the pyroelectric effect, thermo-optic gratings, or surface deformation gratings are found to be negligible as compared to the observed effects [47, 49].
- The build-up of the space-charge grating, as measured in the cw regime in longitudinal geometry, can be described satisfactorily by a double exponential behavior. The associated fast and slow time constants for the recording wavelength $\lambda = 488\,\text{nm}$ are of the order of $10\,\mu\text{s}$ and $100\,\mu\text{s}$, respectively (Y-polarization, $I \approx 0.7\,\text{W/cm}^2$ [47]). At $\lambda = 514\,\text{nm}$, these times become slightly longer.
- The response can be made even faster if the energy deposition is made more rapidly, such as in the case of pulsed excitation. For instance, using 50 ns pulses at 532 nm and a fluence of $100\,\mu\text{J/cm}^2$ (corresponding to the energy deposited in the cw regime during $100\,\mu\text{s}$ at the intensity of $1\,\text{W/cm}^2$), one observes the rise of the diffraction efficiency to its maximum within about $1\,\mu\text{s}$ with a consequent decay (see Fig. 7.8, [45]). Note that if a high pulse repetition rate is necessary, such as in the case described later in Section 7.4.2, it is also important, after the signal peak, to have a quick return of the diffraction efficiency to zero, which is the case here.

To conclude, interband photorefraction in SPS is characterized by fast response times and large nonlinearity as a result of the high electro-optic

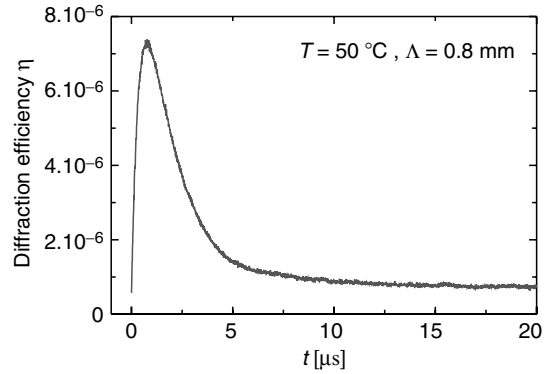

FIGURE 7.8. Dynamics of the diffraction efficiency in $Sn_2P_2S_6$ under pulsed grating recording at 532 nm. Pulse length = 50 ns; Fluence = $100\,\mu\text{J/cm}^2$. (After [45])

coefficients. This is combined with the advantage that the effect can be induced using visible wavelengths, a spectral range where cheaper light sources and compact sources offering a high pulse repetition rate for processing applications are readily available.

4 Applications

Owing to the large absorption constant, interband photorefractive effects are not useful for applications in which the recording light needs to be used further, such as two-wave mixing light amplification and related applications, self-pumped or four-wave mixing phase conjugation, and so on. In contrast, due to the faster dynamics with respect to conventional photorefraction, interband effects are very interesting for applications requiring a large parallel processing speed or a relatively quick switching time.

Four examples are demonstrated here: An optically addressed spatial light modulator (incoherent-to-coherent converter) based on interband photorefraction in $KNbO_3$, a high speed optical correlator based on interband photorefraction in SPS, and again in $KNbO_3$, reconfigurable light induced 1D waveguides with switching times in the 100 μs region, as well as a tunable Bragg filter operating at telecommuncation wavelengths near 1.55 μm.

4.1 High-Speed Optical Processing in $KNbO_3$ *with High Resolution: PICOC*

The fast response time of band-to-band photorefraction, combined with the high resolution proper to short-wavelength light, leads to an extremely high effective parallel processing rate. This may be demonstrated by a photorefractive incoherent to coherent optical converter (PICOC) operated in the interband regime. A PICOC is basically an optically addressed spatial light modulator (SLM) based on the photorefractive effect by which an incoherent wave is transferred onto a coherent beam as illustrated in Fig. 7.9. The information transfer between incoherent and coherent light occurs through diffraction at a modulated holographic phase grating. The latter is the key element that determines the time response and influences the optical resolution. Several implementations making use of conventional photorefraction were demonstrated [50, 51, 52, 53, 54].

An experimental demonstration of a PICOC based on interband photorefractive effects has been performed using a 47 μm thick sample of nominally pure, single domain $KNbO_3$ crystal and the approach schematically depicted in Fig. 7.9 [55]. A very important figure of merit for a incoherent-to-coherent converter is its resolution. In the experimental implementation, an excellent resolution of 124 line pairs/mm (lp/mm) was obtained, which is close to the resolution of 148 lp/mm allowed by the optical system for the incoherent

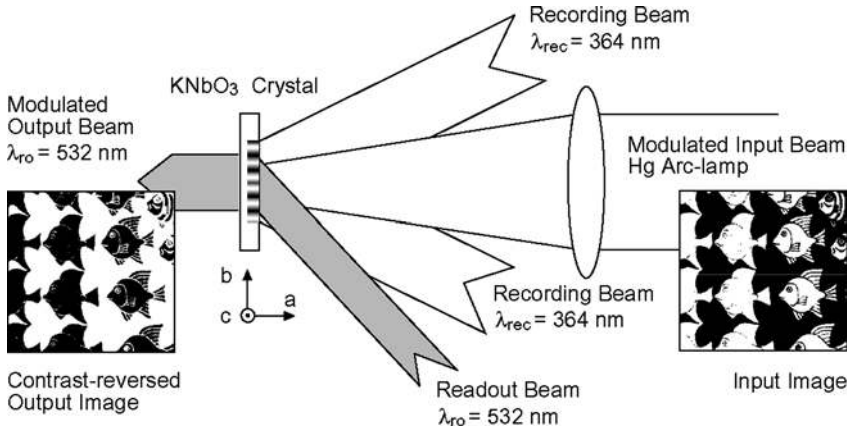

FIGURE 7.9. Principle of a photorefractive incoherent-to-coherent optical converter (PICOC): A projected input image, caried by incoherent light, modulates a superimposed photorefractive Bragg grating that is produced by two interfering recording waves. The (anisotropically) Bragg diffracted read-out laser beam carries the contrast reversed image.

illumination, and to the limiting resolution of 160 lp/mm set by the Bragg diffraction process. The latter depends on the grating thickness and the wavelength used [56, 52].

PICOCs based on interband photorefraction are interesting not only because of the achievable resolution, but obviously, also because of the short build-up and reconfiguration time. For the experimental parameters giving the maximum resolution (recording intensity $= 85\,\mathrm{mW/cm^2}$, average incoherent erasure intensity $= 70\,\mathrm{mW/cm^2}$, read-out intensity $= 5\,\mathrm{W/cm^2}$), a response time of $35\,\mu$s with an overall contrast better than 10:1 was measured. The diffraction efficiency for the read-out wave was $\eta = 0.4\%$.

The intensities mentioned above elucidate another important feature of the interband photorefractive effect. The fact that the gratings are robust against illumination with light of sub band-gap photon energy allows to use very intense read-out waves without affecting the PICOC operation.

The demonstrated write-read-erase cycle was $\tau_c = 70\,\mu$s and represents the achievable frame time. It is possible to combine this with the corresponding resolution and define an incoherent-to-coherent conversion rate by the expression $\Gamma \equiv (2R)^2/\tau_c$, which corresponds to a number of switchable pixels per unit time and unit area. For the PICOC described here, one has $\Gamma = 88\,\mathrm{Gbit}/(s\,cm^2)$, a number rivaled only by optically addressed spatial light modulators based on multiple quantum wells devices [55, 57].

The key performance characteristics mentioned above can be easily extrapolated to other optical processing devices at low intensities such as, for instance, optical correlators. In the next section, we describe a further example where one

makes use of the favorable properties of interband photorefraction for the demonstration of a high repetition rate optical correlator.

4.2 Joint Fourier Transform Correlation

In the past, the speed of optical correlators was often limited by the input electronic interface device, such as the input spatial light modulator (SLM) used in one or both arms of the joint Fourier transform (JFT) scheme first proposed by Weaver and Goodman [58]. Today, the advent of faster display devices such as ferroelectric liquid crystals SLMs has shifted the limiting factor back to the nonlinear device element [59]. It is therefore important to provide a material where the optical processing operation can be performed at a rate at least equal to the input data rate. Among the low-power nonlinear optical effects coming into consideration, the interband photorefractive effect discussed in this chapter is particularly attractive because of the high sensitivity and speed, and because the relatively small thickness of the recorded gratings leads to higher spatial resolution and an increased shift invariance of the correlator.

If an optical correlator has to compete with the steadily improving purely electronic alternatives, its operation frame rate has to be high enough. For electronic correlators, the processing time T required for calculating the correlation between two images of pixel size $N_{\mathrm{px}} \times N_{\mathrm{px}}$ is $T \propto N_{\mathrm{px}}^2 \log_2 N_{\mathrm{px}}$. A JFT optical correlator with 10 kHz frame rate is therefore faster than a 2 GHz clock rate state of the art dedicated digital processor as long as the number of pixels exceeds $N_{\mathrm{px}} \approx 50$.

A system was built to perform fast JFT correlations using $Sn_2P_2S_6$ as nonlinear optical processing element and an angularly multiplexed holographic storage memory [46]. Fig. 7.10 shows the conceptual idea, while a scheme of the setup can be found in the original reference [46]. The system was operated in the pulsed regime using a high repetition rate frequency doubled Nd:YAG laser at the wavelength of 532 nm. The use of the holographic memory permits us to overcome the available speed limitation of the electronic/optic interface device and to operate the JFT correlator at a rate of 10 kHz. As discussed earlier in this chapter, if the holograms performing the correlation operation are being recorded in SPS, the operation can be performed in less than the pulse distance of 100 μs.

The library images were recorded in an angularly multiplexed holographic memory implemented using a thick $LiNbO_3$ crystal. High speed image sequences were produced by reading out 10 phase modulated images of the kind shown on top in Fig. 7.11 at a rate of 10'000 frames/s from the holographic memory. Each image was then compared with an image presently displayed through a ferroelectric liquid crystal spatial light modulator (SLM). The comparison was performed by means of the thin dynamic hologram recorded in real-time in the SPS crystal by the interband photorefractive effect. Two typical correlation traces are shown in Fig. 7.11. The 10 mutual correlation peaks can be clearly identified.

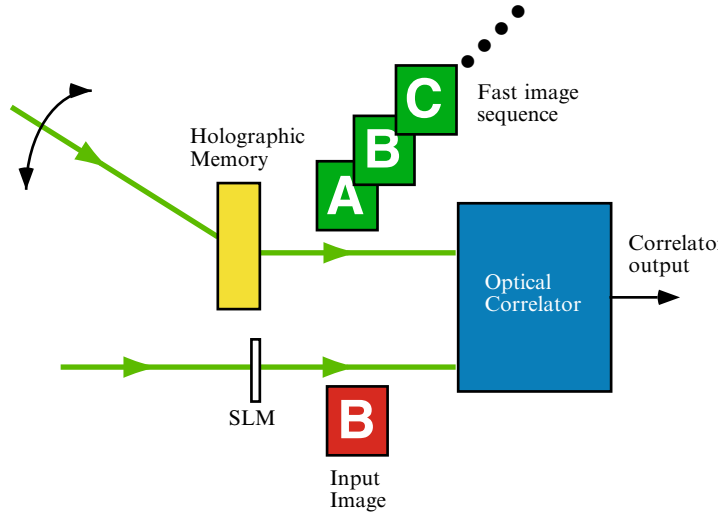

FIGURE 7.10. Principle of operation of a high-rate JFT correlator with an image library stored in a holographic memory.

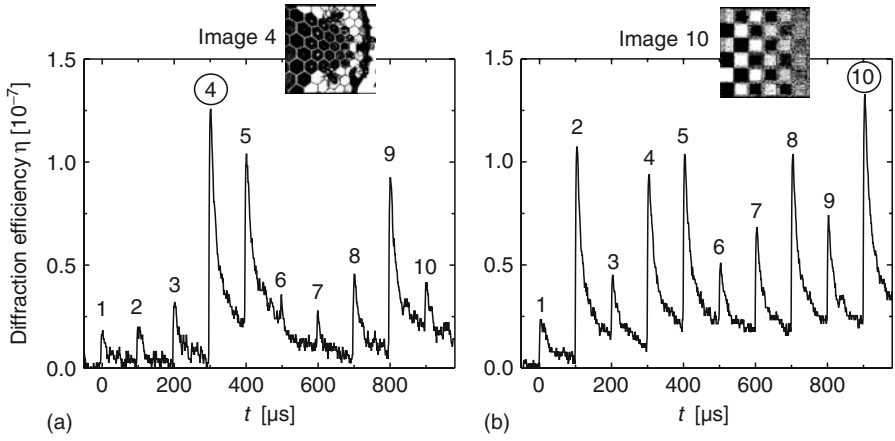

FIGURE 7.11. Intensity of the correlation peaks produced by comparing image 4 (a) and image 10 (b) with an image sequence extracted from the holographic memory at the rate of 10 kHz.

Peak 4 in (a) and peak 10 in (b) are the highest and correspond to the correctly identified displayed images on the SLM.

It can be concluded that, by a combination of a holographic memory with fast dynamic holography, realization of a joint Fourier transform optical correlator working at a frame rate of at least 10 kHz is possible, thus competing

favorably with current electronics. Typical applications of such correlators are pattern and position recognition (fingerprints, faces, industrial tools, objects, ...), tracking of unknown objects or search in large databases of page coded information.

4.3 Light Induced Waveguides

The creation of waveguides that can be dynamically reconfigured at will is a very desirable feature, for instance for applications for optical switching or dynamic optical interconnection. The photorefractive effect, by its own nature, offers the possibility for such reconfigurability. While photorefractive waveguides may be created by several means [60, 61, 62, 63, 64], only the interband photorefractive effect offer the possibility of reconfiguration in the microsecond time range.

The technique discussed here makes use of a controlling beam illuminating the top surface of an electro-optic crystals (pure $KNbO_3$) and imposing the desired waveguide shape [65]. By using interband absorbed light, the latter can be reconfigured in a time of few tens of microseconds with moderate light intensities of the order of $1\,mW/cm^2$. The mechanism underlying waveguide formation is the local screening of an externally applied electric field E, as shown in Fig. 7.12. This is analogous with the mechanisms acting in the case light induced waveguides are produced by beam self-focusing [61] or light induced domain switching [66]. If the light polarization and field direction are chosen properly, the refractive index decreases homogeneously across the sample apart for the regions that are externally illuminated. There the field is screened by bipolar charge transport. Because the desired structure can be

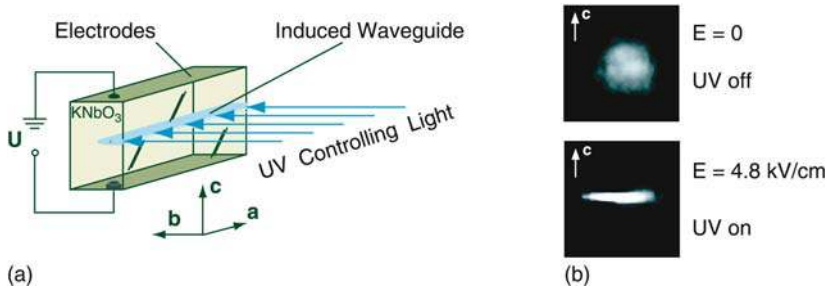

FIGURE 7.12. a. Schematic view of the setup to produce light induced waveguides. An electric field is applied along the c-axis. The controlling UV light, which induces the waveguide, has a photon energy larger than the 3.3 eV bandgap of $KNbO_3$. Due to the strong absorption of UV light in pure $KNbO_3$ (intensity absorption coefficient $\alpha_c = 540 \pm 50\,cm^{-1}$) [11], the UV stripe can induce field screening only for about $150\,\mu m$ below the surface. b. CCD images of the intensity distribution of a HeNe probe beam at the exit face of the crystal (picture size is $240 \times 240\,\mu m$) show the diffracted beam without applied E field and without UV illumination (top), as well as the guided beam for applied E field and with UV illumination (bottom).

imaged onto the surface by a deflector or a photolithographic like process, various waveguide configurations can be easily produced in this way.

With this technique, straight waveguides, Y-branches, and 1×4 and 1×8 connectors have been demonstrated [67] for guiding red probe light as well as light at the telecommunication wavelengths of 1.3 and 1.55 μm. Obviously, due to the larger natural diffraction, larger fields are required to achieve the same waveguide width in this case. The guided beam full-width-at-half maximum scales roughly as $\lambda/E^{1/2}$. Note that the guiding properties are found to be unchanged as the intensity of a HeNe probe beam is increased from 0.004 to 200 $\mathrm{W/cm^2}$, confirming therefore the robustness of refractive-index changes induced by band-to-band photorefraction. The total losses in the induced waveguide correspond to an intensity loss coefficient $\alpha < 0.02\,\mathrm{cm^{-1}}$, i.e., less than 0.1 dB/cm.

On the base of the method described above, attractive all-optical devices may be created, such as switches, real time beam deflectors, tunable Y-branches, or reconfigurable optical interconnects compatible with telecommunication wavelengths. Alternatively such low loss light induced waveguides might be used also in connection with nonlinear optical frequency conversion.

4.4 Tunable Bragg Filters

In wavelength division multiplexing (WDM) and dense WDM (DWDM) systems, tunable optical filters are needed to manipulate or select a desired wavelength from the band of available channels and a suitable tunable optical filter needs both a large tuning range and a narrow bandwidth. Among the various possible approaches [68, 69], tunable filters based on volume holograms offer the important advantage of a very high wavelength selectivity of the filter [70, 71].

Interband photorefraction in pure $KNbO_3$ were used in [71] to implement dynamic narrow-bandwidth thick holographic reflection gratings for telecommunication wavelengths near 1550 nm. The tuning can be done in microseconds and is achieved by using an acousto-optic deflector to control the direction of the recording beams and hence the spacing of the photorefractive gratings, as shown in Fig. 7.13. A bandwidth of 0.13 nm and fast tuning between channels spaced by 50 GHz frequency were demonstrated.

Any crystal that exhibits interband photorefractive effect could be used for such a task instead of $KNbO_3$: In particular materials like $Sn_2P_2S_6$ where interband photorefraction at visible recording wavelengths is possible, as discussed in Section 7.3.3.

5 Conclusions

In this chapter, we have given a short introduction to interband photorefractive effects and described them by a simple model for the limiting case of neglecting any mid-band-gap states. The principal advantages of interband photorefraction are the much faster response speeds than achievable through conventional

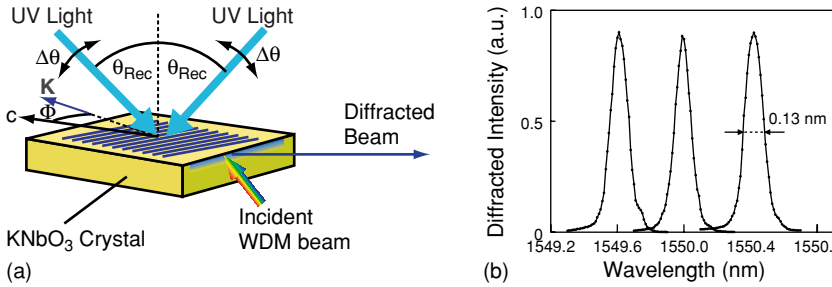

FIGURE 7.13. (a) Principle of a tunable optical filter by volume holography. The Bragg wavelength of the filter is tuned by changing the mutual angle $2\theta_{Rec}$ between the interfering writing beams symmetrically. This induces a change of the grating constant but no change in the direction of the grating vector K. From the multiple wavelengths of an incident WDM beam only the one corresponding to the Bragg wavelength of the grating is diffracted if the filter's bandwidth is smaller than the WDM channel spacing. (b) Wavelength selectivity scan for three different grating vectors separated by 0.4 nm (50 GHz). The three peaks are obtained by using three different grating constants. (After [71])

photorefraction, and the great robustness of the induced refractive index variations against erasure with light at longer wavelengths.

On the other hand, the drawbacks of interband photorefractive effects are related with the large absorption constant. Any application where the recording light has to be reused or detected after the nonlinear material is better performed using conventional photorefractive effects. Examples of such applications can be found in the fields of holographic storage, adaptive interferometry, coherent image amplification, laser beam cleanup, and phase conjugation. Many of these examples are discussed in this book series. If, in contrast, the recording light can be fully sacrificed in the nonlinear sample, one is better off by using the interband processes.

Three electro-optic materials, $KNbO_3$, $LiTaO_3$, and $Sn_2P_2S_6$ have been discussed in more detail. In the first material, the band-to-band processes occur at near ultraviolet wavelengths; in the second one, at deep ultraviolet wavelengths; in the third one, they occur already in the blue-green spectral region. For $KNbO_3$ and $Sn_2P_2S_6$, response times of a few μs can be achieved at conventional cw intensity levels, while response times for $LiTaO_3$ are in the few ms region for near-stoichiometric crystals and slightly faster than 1 ms for Mg doped near stoichiometric $LiTaO_3$. Due to the speed of response, the interband photorefractive effect is interesting for applications in fast parallel optical processing. Examples of an optically addressed spatial light modulator and of a Joint Fourier transform optical correlator were given. Other examples were given in connection with the manipulation and guiding of an optical beam by means of a controlling light pattern, and with the recording of dynamically reconfigurable narrow-bandwidth holographic reflection gratings for wavelength filtering.

The existence of interband photorefractive effects is not expected to be limited to the materials discussed here; depending on the required wavelength of operation, other electro-optic compounds may be selected and investigated in this context.

References

1. G.C. Valley, T.F. Boggess, J. Dubard, A.L. Smirl, J. Appl. Phys. **66**, 2407 (1989).
2. A. Partovi, A. Kost, E. Garmire, G.C. Valley, M.B. Klein, Appl. Phys. Lett. **56**, 1089 (1990).
3. V.W. Franz, Z. Naturforschg. **13a**, 484 (1958).
4. L.V. Keldysh, Soviet Phys. JETP **34**, 788 (1958).
5. D.D. Nolte, D.H. Olson, G.E. Doran, W.H. Knox, and A.M. Glass, J. Opt. Soc. Am. B **7**, 2217 (1990).
6. D.A. Miller, D.S. Chemla, T.C. Damen, A.C. Goddard, W. Wiegmann, T.H. Wood, and C.A. Burrus, Phys. Rev. Lett. **53**, 2173 (1984).
7. D.D. Nolte and R.M. Melloch, in *Photorefractive Effects and Materials, Electronic Materials: Science and Technology*. pp. 373–451 edited by D. D. Nolte, Kluwer Academic Publishers, Boston (1995).
8. E. Garmire, IEEE J. Sel. Topics QE **6**, 1094 (2000).
9. D. Von der Linde, A.M. Glass, and K.F. Rodgers, Appl. Phys. Lett. **25**, 155 (1974).
10. D. Von der Linde, A.M. Glass, and K.F. Rodgers, Appl. Phys. Lett. **26**, 22 (1975).
11. G. Montemezzani, P. Rogin, M. Zgonik, and P. Günter, Phys. Rev. B **49**, 2484 (1994).
12. N.V. Kukhtarev, V.B. Markov, S.G. Odulov, M.S. Soskin, and V.L. Vinetskii, Ferroelectrics **22**, 949 (1979).
13. P. Bernasconi, G. Montemezzani, I. Biaggio, and P. Günter, Phys. Rev. B **56**, 12196 (1997).
14. P. Bernasconi, Dissertation, Diss. ETH No. 12761, Swiss Federal Institute of Technology, Zürich (1998).
15. P. Bernasconi, G. Montemezzani, and P. Günter, Appl. Phys. B **68**, 833 (1999).
16. G. Montemezzani, P. Rogin, M. Zgonik, and P. Günter, Opt. Lett. **18**, 1144 (1993).
17. M. Ewart, M. Zgonik, and P. Günter, Opt. Commun. **141**, 99 (1997).
18. M. Carrascosa, F. Agullo-Lopez, G. Montemezzani, and P. Günter, Appl. Phys. B **72**, 697 (2001).
19. G. Montemezzani, P. Bernasconi, Ph. Dittrich, R. Ryf, and P. Günter, Proc. SPIE **4358**, 1 (2001).
20. H.J. Eichler, P. Günter, and D.W. Pohl, *Laser-induced dynamic gratings*, Springer Verlag, Berlin (1986).
21. N. Kukhtarev, T. Kukhtareva, and P. P. Banerjee, Proc. IEEE **87**, 1857 (1999).
22. S. Ducharme, Opt. Lett. **16**, 1791 (1991).
23. K. Buse, J. Opt. Soc. Am. B **10**, 1266 (1993).
24. F. Jermann, M. Simon, and E. Krätzig, J. Opt. Soc. Am. B **12**, 2066 (1995).
25. L. Kovács, G. Ruschhaupt, K. Polgár, G. Corradi, and M. Wöhlecke, Appl. Phys. Lett. **70**, 2801 (1997).
26. Y. Furukawa, K. Kitamura, E. Suzuki, and K. Niwa, J. Crystal Growth **197**, 889 (1999).

27. P. Bernasconi, G. Montemezzani, P. Günter, Y. Furukawa, and K. Kitamura, Ferroelectrics **223**, 373 (1999).
28. Y. Furukawa, K. Kitamura, K. Niwa, H. Hatano, P. Bernasconi, G. Montemezzani, and P. Günter, Jpn. J. Appl. Phys. **38**, 1816 (1999).
29. M. Jazbinšek, M. Zgonik, S. Takekawa, M. Nakamura, K. Kitamura, and H. Hatano, Appl. Phys. B **75**, 891 (2002).
30. Ch. Bäumer, C. David, A. Tunyagi, K. Betzler, H. Hesse, E. Krätzig, and M. Wöhlecke, J. Appl. Phys. **93**, 3102 (2003).
31. Ph. Dittrich, B Koziarska-Glinka, G. Montemezzani, P. Günter, S. Takekawa, K. Kitamura, and Y. Furukawa, J. Opt. Soc. Am. B **21**, 632 (2004).
32. Ph. Dittrich, G. Montemezzani, M. Habu, M. Matsukura, S. Takekawa, K. Kitamura, and P. Günter, Opt. Commun. **234**, 131 (2004).
33. F. Nitanda, Y. Furukawa, S. Maiko, M. Sato, and K. Ito, Jpn. J. Appl. Phys. I **34**, 1546 (1995).
34. M. Nakamura, S. Takekawa, K. Terabe, K. Kitamura, T. Usami, K. Nakamura, H. Ito, and Y. Furukawa, Ferroelectrics **273**, 199 (2002).
35. Y. Furukawa, K. Kitamura, S. Takekawa, K. Niwa, and H. Hatano, Opt. Lett. **23**, 1892 (1998).
36. G.Q. Zhang, G.Y. Zhang, S.M. Liu, J.J. Xu, Q. Sun, and X.Z. Zhang, J. Appl. Phys. **83**, 4392 (1998).
37. J. Xu, G. Zhang, F. Li, X. Zhang, Q. Sun, S. Liu, F. Song, Y. Kong, X. Chen, H. Qiao, J. Yao, and Z. Lijuan, Opt. Lett. **25**, 129 (2000).
38. D. Haertle, G. Caimi, A. Haldi, G. Montemezzani, P. Günter, A. A. Grabar, I.M. Stoika, and Yu. M. Vysochanskii, Opt. Commun. **215**, 333 (2003).
39. A.A. Grabar, Ferrolelectrics **170**, 133 (1995).
40. S.G. Odoulov, A.N. Shumelyuk, U. Hellwig, R.A. Rupp, and A.A. Grabar, Opt. Lett. **21**, 752 (1996).
41. S.G. Odoulov, A.N. Shumelyuk, U. Hellwig, R.A. Rupp, A.A. Grabar, and I.M. Stoyka, J. Opt. Soc. Am. B **13**, 2352 (1996).
42. A.A. Grabar, I.V. Kedyk, M.I. Gurzan, I.M. Stoika, A.A. Molnar, and Y.M. Vysochanskii, Opt. Commun. **188**, 187 (2001).
43. A. Shumelyuk, S. Odoulov, D. Kip, and E. Krätzig, Appl. Phys. B **72**, 707 (2001).
44. M. Jazbinsek, G. Montemezzani, P. Günter, A.A. Grabar, I.M. Stoika, and Yu. M. Vysochanskii, J. Opt. Soc. Am. B **20**, 1241 (2003).
45. R. Ryf, G. Montemezzani, P. Günter, A.A. Grabar, I.M. Stoika, and Y.M. Vysochanskii, Trends Opt. Photon. **62**, 11 (2001).
46. R. Ryf, G. Montemezzani, P. Günter, A.A. Grabar, I.M. Stoika, and Yu. M. Vysochanskii, Opt. Lett. **26**, 1666 (2001).
47. G. Montemezzani, R. Ryf, D. Haertle, P. Günter, A.A. Grabar, I.M. Stoika, and Yu, M. Vysochanskii, Ukr. J. Phys. **49**, 333 (2004).
48. R. Mosímann and D. Haertle, Private Communication.
49. R. Ryf, Dissertation, Diss. ETH No. 13546, Swiss Federal Institute of Technology, Zürich (2000).
50. A.A. Kamshilin and M.P. Petrov, Sov. Tech. Phys. Lett. **6**, 144 (1980).
51. Y. Shi, D. Psaltis, A. Marrakchi, and A.R. Tanguay, Appl. Opt. **22**, 3665 (1983).
52. P. Amrhein and P. Günter, J. Opt. Soc. Am. B **12**, 2387 (1990).
53. J.S. Zhang, H.T. Wang, S. Yoshikado, and T. Aruga, Opt. Lett. **22**, 1612 (1997).
54. J.S. Zhang, H.T. Wang, S. Yoshikado, and T. Aruga, Appl. Opt. **38**, 995 (1999).

55. P. Bernasconi, G. Montemezzani, M. Wintermantel, I. Biaggio, and P. Günter, Opt. Lett. **24**, 199 (1999).
56. A. Marrakchi, A.R. Tanguay, J. Yu, and D. Psaltis, Opt. Eng. **24**, 124 (1985).
57. S.R. Bowman, W.S. Rabinovich, G. Beadie, S.M. Kirkpatrick, D.S. Katzer, K. Ikossi-Anastasiou, and C.L. Adler, J. Opt. Soc. Am. B **15**, 640 (1998).
58. C.S. Weaver and J.W. Goodman, Appl. Opt. **5**, 1248 (1966).
59. J. Colin, N. Landru, V. Laude, S. Breugnot, H. Rajbenbach, and J.P. Huignard, J. Opt. A: Pure Appl. Opt. **1**, 283 (1999).
60. K. Itoh, O. Matoba, and Y. Ichioka, Opt. Lett. **19**, 652 (1994).
61. M.F. Shih, Z.G. Chen, M. Mitchell, M. Segev, H. Lee, R.S. Feigelson, and J.P. Wilde, J. Opt. Soc. Am. B **14**, 3091 (1997).
62. O. Matoba, T. Inujima, T. Shimura, and K. Kuroda, J. Opt. Soc. Am. B **15**, 2006 (1998).
63. D. Kip, Appl. Phys. B **67**, 131 (1998).
64. O. Matoba, K. Itoh, and K. Kuroda, Proc. IEEE **87**, 2030 (1999).
65. Ph. Dittrich, G. Montemezzani, P. Bernasconi, and P. Günter, Opt. Lett. **24**, 1508 (1999).
66. A. Bekker, A. Peda'el, N.K. Berger, M. Horowitz, and B. Fischer, Appl. Phys. Lett. **72**, 3121 (1998).
67. Ph. Dittrich, Dissertation, Diss. ETH No. 15414, Swiss Federal Institute of Technology, Zürich (2004).
68. H. Kobrinski and K.-W. Cheung, IEEE Commun. Mag. **27**, 53 (1989).
69. D. Sadot and E. Boimovich, IEEE Commun. Mag. **36**, 50 (1998).
70. V.M. Petrov, C. Denz, A.V. Shamray, M.P. Petrov, and T. Tschudi, Opt. Mater. **18**, 191 (2001).
71. Ph. Dittrich, G. Montemezzani, and P. Günter, Opt. Commun. 214, 363 (2002).